Iğdır Üniversitesi Fen Bilimleri Enstitüsü Dergisi, 11(1): 240-257, 2021
Journal of the Institute of Science and Technology, 11(1): 240-257, 2021
ISSN: 2146-0574, eISSN: 2536-4618

Fizik / *Physics* **DOI: 10.21597/jist.792023**

Araştırma Makalesi / *Research Article*

Geliş tarihi / Received: 08-09-2020 **Kabul tarihi / Accepted: 01-10-2020**

Frequency Dependence of Dielectric, Conductivity, Impedance and Electrical Modulus Properties of La^{3+} Substituted in Cobalt- Magnesium Ferrites

Tuğba ŞAŞMAZ KURU[1*]

ABSTRACT: In this study, structural, morphological, dielectric and AC conductivity properties of CoMgLa ferrite samples ($Co_{0.5}Mg_{0.5}La_xFe_{2-x}O_4$) were investigated according to the change of x (x=0, 0.1, 0.2, 0.3, 0.4 and 0.5). Samples were synthesized by co-precipitation method. The structural properties were examined using XRD and results show that the prepared sample crystallizes in the cubic spinel structure. Crystallite sizes are changing between 24.92 to 9.80 nm. Morphological and elemental properties were analyzed by SEM and EDX. Dielectric properties were investigated by impedance spectroscopy. The samples showed normal dielectric properties consistent with the Maxwell-Wagner model due to interfacial polarization. When the impedance characteristics were examined, it was found that the relaxation process was compatible with the Cole-Cole model. The results of the modulus show that grains contribute to the relaxation process as well as grain boundaries. AC conductivity exhibited semiconductor behavior. The constant behavior of conductivity at low frequencies is a sign that the examined samples may be suitable for many applications.

Keywords: La^{3+} substituted Co-Mg ferrites, Dielectric properties, Impedance, Modulus, AC conductivity.

[1]Tuğba ŞAŞMAZ KURU (**Orcid ID:** 0000-0002-3200-487X), İstanbul Okan University, Vocational School of Health Services, İstanbul, Turkey

*Sorumlu Yazar/Corresponding Author: Tuğba ŞAŞMAZ KURU, e-mail: tugbasasmaz191@gmail.com

INTRODUCTION

Ferrite materials play an important role in technological applications with their structural, optical, electrical and magnetic properties (Ashtar et al., 2016). The examination of these materials in nano scale is important in terms of experimental and theoretical adaptation to various application areas (Ashtar et al., 2016). These application areas of ferrite nanoparticles are very broad, including military, space technology, magnetic drug delivery, cancer treatment, magnetic resonance imaging, gas and humidity sensors etc. (Shinde et al., 2010; Köseoğlu et al., 2012; Ciocarlan et al., 2016; Safi et al., 2016; Sutka and Gross, 2016; Şaşmaz Kuru and Şentürk, 2016). Ferrites has also been studied because of their high dielectric constant, high magnetic permeability, very low dielectric loss over a wide frequency range and remarkable chemical stability (Ishaque et al., 2015; Pawar et al., 2016; Mazen and Abu-Elsaad, 2017). In order to use electrical transport and dielectric properties in high frequency applications, real part of dielectric function (ε′), imaginary part of dielectric function (ε", dielectric loss), dielectric loss tangent (tanδ) and AC electrical conductivity (σ_{ac}) parameters should be examined. (Ghodake et al., 2017). As is known, these properties are directly related to the production methods of the ferrites (Ramesh et al., 2016).

The general formula of spinel ferrites is MFe_2O_4 where M is a divalent metal cation. The chemical and physical properties of spinel ferrites can be changed in generally by changing divalent cations without altering the crystal structure (Li et al., 2017). Ferrites unit cells consist of A and B sites. These sites are also called tetrahedral and octahedral sites. Each unit cell has 64 tetrahedral sites and 32 octahedral sites (Ghodake et al., 2016). M^{2+} and Fe^{3+} ions are distributed in these sites (Manikandan et al., 2015). This distribution between the two sites affects the magnetic properties of the materials (Thomas et al., 2017). Ferrites can be produced by many different production methods such as; sol-gel [8], chemical co-precipitation method (Şaşmaz Kuru et al., 2017), solid state reaction route (Vasoya et al., 2016), oxalate precursor chemical method (Ghodake et al., 2016). Size and properties of ferrite particles may change with preparation conditions. These conditions include the pH degree, the fuel used for synthesis, stirring temperature, stirring time, stirring speed, and the rates of metal nitrate used (Raut et al., 2015). In previous years, Co-Mg ferrite has been produced with different production methods by substituted metals such as Cr, Cu, Al, Zn, Ni etc. with various stoichiometric ratios and their dielectric and conductivity properties, especially their structural and magnetic properties have been investigated (Ahmad et al., 2014; Patil et al., 2014; Gao et al., 2015; Kaur et al., 2015; Sharma et al., 2015; Mund and Ahuja, 2017; Jadoun et al., 2018; Ramarao et al., 2018; Sun et al., 2018). Also, there are investigations of La-Mg and La-Co mixed ferrites in the literature separately (Yang et al., 2018; Gaba et al., 2018). Since the La^{3+} ion is less paramagnetic, an increase in DC resistance occurs at room temperature when substituted with iron (Ahmed et al., 2005; Ikram et al., 2018) With this feature, it is envisaged to be used for gas sensors, metal catalysts, energy and data storage systems by increasing the magnetic and dielectric parameters. However, La^{3+}-doped Co-Mg ferrite studies have not been examined according to best of our knowledge except for the previous work of the author (Köseoğlu et al., 2016).

In this paper, a series of La^{3+} substituted Co-Mg ferrites ($Co_{0.5}Mg_{0.5}La_xFe_{1-x}O_4$, x = 0, 0.1, 0.2, 0.3, 0.4 and 0.5) were synthesized by co-precipitation method. This method has been chosen for production because of its simple, inexpensive and environmentally friendly properties (Sharma et al., 2016; Şaşmaz Kuru et al., 2018). Also, the effects of La^{3+} doping amount on the structure and dielectric properties of samples were studied in detail. Structural properties of the samples were investigated with X-Ray diffractometer (XRD) and morphological properties were investigated with scanning electron

microscope (SEM) techniques. Dielectric and conduction mechanism were studied in the frequency range of 20 Hz to 10 MHz at room temperature.

MATERIALS AND METHODS

Materials

In this study, deionized water was used as a fuel and dissolvent agent for starting elements of $Co(NO_3)_2.6H_2O$, $Mg(NO_3)_2$, $La(NO_3)_2$, $Fe(NO_3)_3.9H_2O$ that were purchased from Merck, Germany (>99.0 %).

Experimental procedure

Adsorption La^{3+} doped Co-Mg ferrites were prepared by co-precipitation method with stoichiometric composition of $Co_{0.5}Mg_{0.5}La_xFe_{1-x}O_4$ (x=0, 0.1, 0.2, 0.3, 0.4 and 0.5). In this study, deionized water was used as a fuel and dissolvent agent for starting elements of $Co(NO_3)_2.6H_2O$, $Mg(NO_3)_2$, $La(NO_3)_2$, $Fe(NO_3)_3.9H_2O$ that were purchased from Merck, Germany (>99.0 %). The required amount of salt has been dissolved in 10 ml deionized water for all samples. The solution was continuously stirred to homogenize with a magnetic stirrer in a water bath which has been heated. When the solution temperature reached 80ºC, 2M NaOH added. The addition of NaOH at pH control was interrupted when the pH reached 11-12. Brown precipitate was obtained. The precipitates were washed several times and filtered through filter paper to remove impurities and contaminations. The precipitates were dried overnight at 105°C in an oven. Finally, the precipitate was calcined at 800ºC for 8 hours.

The obtained powders were pelleted under 3 tons of pressure for dielectric and electrical measurements. These pellets, with ~2.5 mm thickness and ~14 mm diameter, were sintered at 1100ºC for 5 hours. Both surfaces of the pellets were sanded to get rid of their roughness. The smooth surfaces were coated with silver conductive paint to role as an electrode in the measurements. The whole experimental procedure is summarized in Fig. 1.

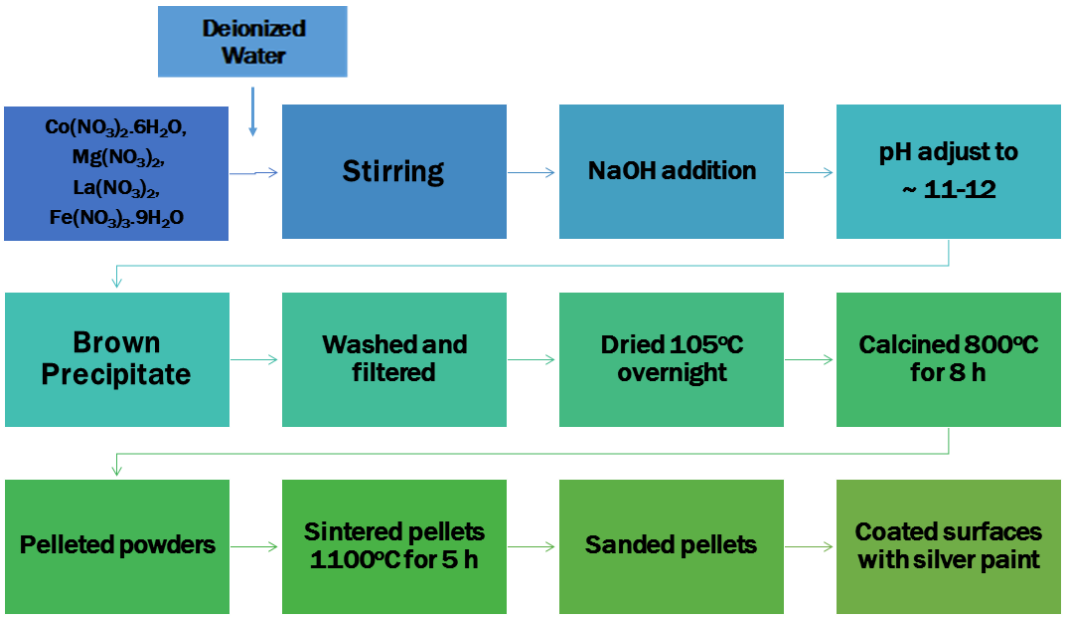

Figure.1. Fabrication steps of the CoMgLa ferrites

Characterization

XRD analysis was performed with an X-ray diffractometer (Rigaku D/Max/2200/PC model device) using Cu-Kα radiation (λ = 1.54050 A°) with a $1^{\circ}min^{-1}$ scanning speed in the 2θ range between 20˚ and 80˚ operating at under 40 kV voltage and 30 mA current. The morphology and microstructures of the CoMgLa ferrites were characterized by a scanning electron microscope (SEM, model JEOL-JSM 6060 LV) at an acceleration voltage of 20 kV. Dielectric and conductivity measurements were carried on by using GW Instek LCR-meter (8110G, parallel plate) in the frequency range of 20 Hz to 10 MHz at room temperature.

RESULTS AND DISCUSSION

Structural results

Adsorption X-ray diffraction patterns of CoMgLa samples in the 2θ range between 10º and 90º with step size of 0.01º are shown in Fig. 2. It can be observed that all the diffraction peaks for each sample were well conformed to the standard diffraction peaks of spinel ferrites with cubic spinel structure ((111), (220), (311), (222), (400), (422), (511) and (440), JCPDS 036-0398). However, with the addition of the La^{3+} additive, the peaks of the $LaFeO_3$ phase ((101), (121), (220), (202), (240), (242) and (204)) were evident along with the increased amount of x. Similar to the studies in the literature, $LaFeO_3$ peak intensities became stronger in parallel with the contribution of La^{3+} (Huang et al., 2014; Wu et al., 2015). With the increasing contribution of La^{3+}, the peak intensity decreased, and the peak width increased. The crystallite sizes were calculated using the Debye-Scherrer equation (Eq. 1), where D is crystalline size, λ is the wavelength of X-ray, β is the line broadening at half maximum intensity (FWHM) and diffraction angle is θ. Lattice parameter of the examined samples values calculated using the Eq. 2, where h, k and l are the Miller indices. Cell volumes (V) of the samples calculated from lattice parameters (a) using the Eq. 3. The theoretical (X_{ray}) densities were calculated from the molecular weight and the cell volume in Eq. 4, where M is the molecular weight of the sample and N_a is Avogadro number (6.02×10^{23}). The masses and volumes of the samples were used to calculate the actual densities in Eq. 5, where r is the radius of the pellets and h is the height of the pellets. Porosity and specific surface area of CoMgLa samples were calculated with the help of Eq. 6, and Eq. 7, respectively. All formulas are listed below (Kuru et al., 2019):

$$D = \frac{0.8\lambda}{\beta \cos\theta} \quad (1)$$

$$a = \frac{\lambda\sqrt{h^2+k^2+l^2}}{2\sin\theta} \quad (2)$$

$$V = a^3 \quad (3)$$

$$d_x = \frac{8M}{N_a V} \quad (4)$$

$$d_{bulk} = \frac{m}{V} = \frac{m}{\pi r^2 h} \quad (5)$$

$$P = 1 - \frac{d_{bulk}}{d_x} \quad (6)$$

$$S = \frac{6}{d_x D} \quad (7)$$

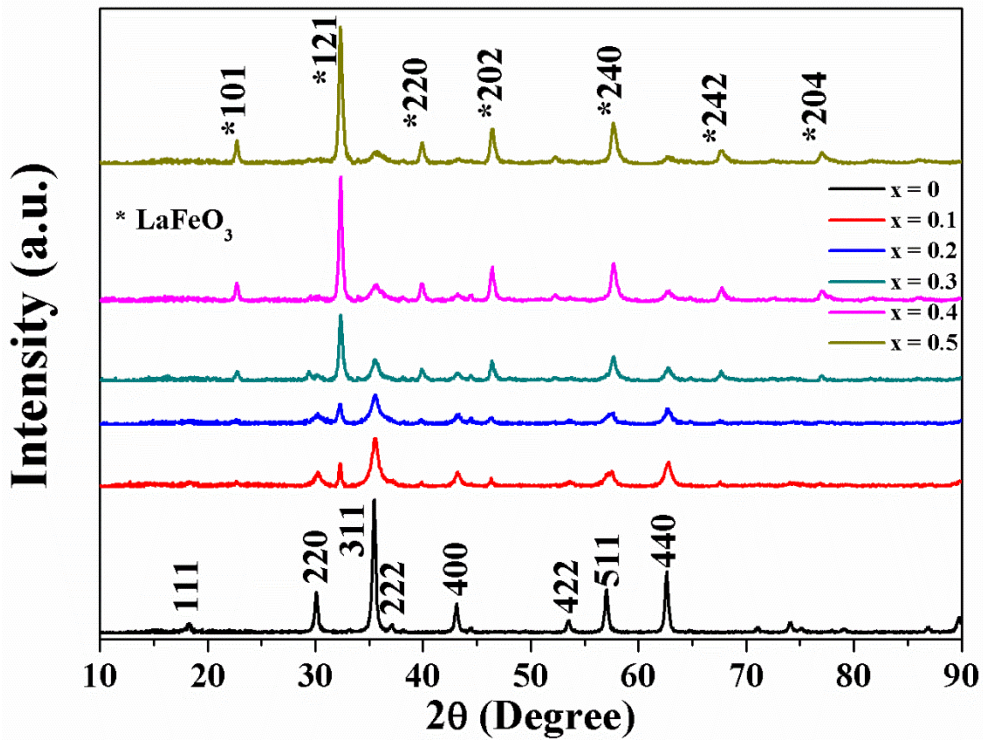

Figure.2. XRD pattern of the CoMgLa ferrite

The structural results of the samples are shown in the Table 1. The crystal sizes of CoMgLa samples - decrease with increasing amount of La^{3+}. These slight decrease in crystallite size with the substitution of lanthanum ions in cobalt-magnesium ferrite results in increase in the surface area. This is associated with nucleation and particle growth (Godlyn Abraham et al., 2018). Also, it is known that, the particle growth depends on the grain boundaries, mobility, grain growth etc. (Jadhav et al., 2019). By increasing the contribution of La^{3+}, the decrease in grain growth can be attributed to the distinction of grain boundaries. This causes the blockage of the movement (Rao et al., 2016). As can be seen from the table, the lattice constant increases with increasing contribution of La^{3+}. In the octahedral sites, the replacement of Fe^{3+} ions with La^{3+} ions cause the expansion of the unit cell, resulting in larger lattice constants. This can be explained by the fact that the radius of the La^{3+} ions (1.061 Å) is greater than the radius of the Fe^{3+} ions (0.67 Å) (Ren and Xu, 2014). The increase in the lattice volume usually leads to an increase in the diffusion pathway, resulting in an increase in the rate of diffusion between the cations in the solid solution (Druce et al., 2014). X-ray and bulk densities of the samples are shown in Table 1. It was found that the X-ray density, increased linearly from 4.94 to 5.85 g/cm^3 with increase in La^{3+} concentration. This increase was due to the larger radius of the La^{3+} as compared to the Fe^{3+} ions. As can be seen from the Table 1, X-ray densities are greater than bulk densities for all samples. This difference is a result of the porous structure of the growing sample during sintering or production (Rafiq et al., 2015).

Table 1 The crystallite size (D), lattice parameter (a), cell volume (V), X-ray density (d_x), bulk density (d_{bulk}), porosity P (%) and specific surface area (S) values of the samples.

x	Crystallite Size D (nm)	Lattice Constant a (A°)	Cell Volume $V(A^o)^3$	X ray Density d_x (g/cm^3)	Bulk Density d_{bulk} (g/cm^3)	Porosity (%)	Specific Surface Area S (m^2/g)
0	24.62	8.3556	583.355	4.95	3.33	33	49.23
0.1	14.32	8.3602	584.319	5.11	3.91	23.5	81.99
0.2	13.95	8.3648	585.284	5.31	3.52	33.7	81.00
0.3	12.97	8.3657	585.472	5.49	3.63	34.2	84.26
0.4	10.92	8.3693	586.229	5.68	3.51	38.2	96.73
0.5	9.80	8.3817	588.838	5.84	3.75	35.8	104.83

To determine the physical and electrical properties of the ferrites, it is important to examine the morphology and grain shapes of the samples (Şaşmaz Kuru and Şentürk, 2016; Kuru et al., 2019). Micrographs of CoMgLa samples sintered at 1100°C are shown in Fig. 3. As seen from the SEM micrographs, the samples consist of irregularly shaped nano-sized particles. In some regions, agglomerations were detected. The agglomeration of the nanoparticles can be attributed to the presence of the surface tension phenomenon of the interface (Sundararajan et al., 2017). Differences in particle sizes between samples in SEM images may be related to agglomerations and accumulation due to the magnetic structure of the samples as a result of stoichiometry combinations. The grain sizes observed with SEM images were found to be larger than the grain sizes obtained from the XRD results. The reason for this difference may be agglomerations and accumulation, as well as the melting of the surfaces of the particles during sintering (Sharma et al., 2015).

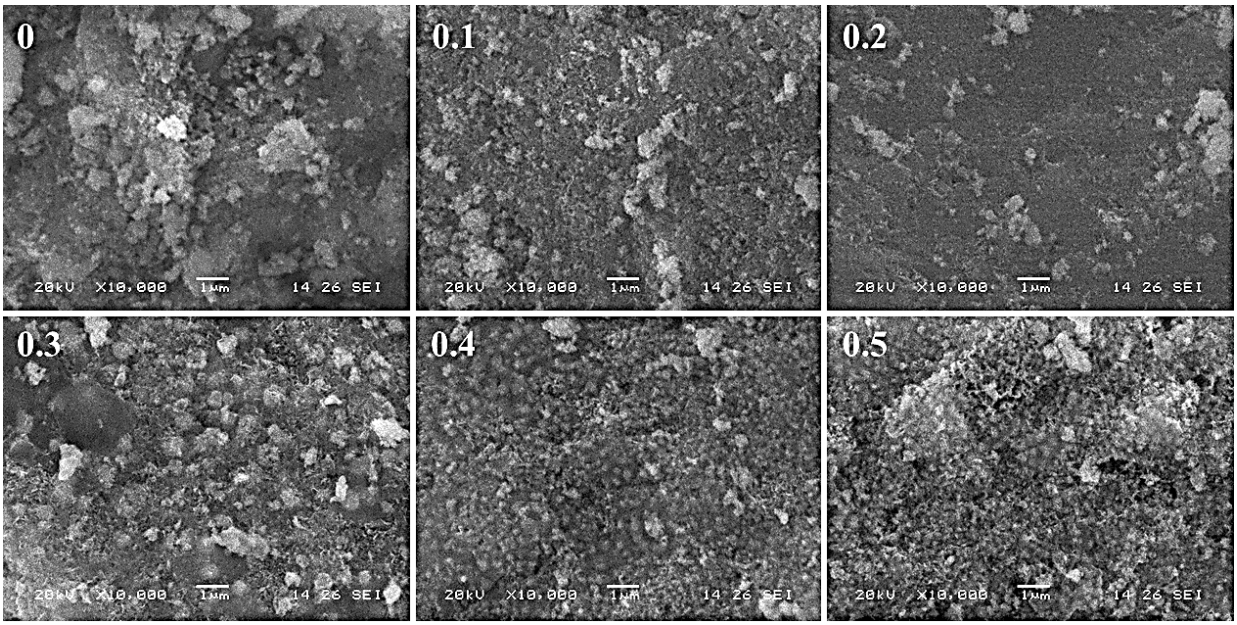

Figure.3. SEM micrographs of CoMgLa ferrites for all compositions

EDX analysis is a method used to examine the elemental distribution of samples. From EDX results shown in Table 2, presence of the constituent elements La, Fe, Co, Mg, and O has been observed in different La^{3+} concentration in CoMgLa ferrites without impurities. Thus, it is understood that the samples examined have the desired stoichiometry. While x = 0, La was not theoretically expected, nor was it observed in experimental results. As the x value increases, the increase of La amount is clearly

observed. The calculated and observed atomic percentages are almost equal, that verifies the contents of the produced samples.

Table 2 The calculated and observed atomic percentages of the examined samples.

Atomic %							
		0	**0.1**	**0.2**	**0.3**	**0.4**	**0.5**
Exp	**Co**	14.190	13.387	12.991	12.192	11.898	11.850
	Mg	4.835	4.326	4.717	4.824	4.700	4.334
	La	-	5.945	11.451	16.577	22.796	26.466
	Fe	51.329	48.937	43.283	39.946	35.005	32.705
	O	29.646	27.405	27.557	26.461	25.601	24.644
Calc.	**Co**	13.560	13.062	12.600	12.175	11.761	11.383
	Mg	5.592	5.387	5.195	5.021	4.850	4.695
	La	-	6.158	11.877	17.518	22.178	26.836
	Fe	51.398	47.037	42.968	39.225	35.625	32.362
	O	29.450	28.370	27.360	26.442	25.544	24.712

Electrical properties

In order to obtain the dielectric and conductivity parameters, capacitance (C) and conductance (G) values were measured in the frequency range of 20 Hz and 10 MHz at room temperature. The dielectric constant values were obtained from the measured capacitance data using the following formula:

$$\varepsilon' = \frac{Cd}{A\varepsilon_0} \tag{8}$$

where d is the thickness of the pellet, A is the surface area of the pellet, and ε_0 is the dielectric permittivity of free space.

The variations of the real part of dielectric function with frequency for all concentrations is shown in the Fig. 4. As can be clearly seen from the figure, the real dielectric constant decreases with increasing frequency and become almost constant, while it increases with increasing x concentration in almost all frequency values. This reduction with frequency is attributed to the fact that the dielectric structure consists of electrically poor grain boundaries and well conductive grains (Kumar et al., 2013). The reduction of the high real dielectric constant at low frequencies with increasing frequency is compatible with Maxwell-Wagner's two-layer model (Raut et al., 2015). At this model, while grain boundaries are effective at low frequencies, conductive grains are active at high frequencies.

The change in real dielectric constant is also explained by the space-charge polarization, which creates a local charge accumulation under the electric field. This polarization is due to the heterogeneity of the dielectric structure in the grain boundaries (Şaşmaz Kuru et al., 2018). Iron ions, which are commonly found on B sites, are assumed to be the cause of polarization in the octahedral regions due to the electronic hopping. Polarization on the tetrahedral sites is caused by hole hopping. Reduction of the real dielectric constant with increasing frequency results from the fact that the polarization could not go beyond a certain frequency with the applied alternative field. This is an expected behavior for ferrites (Naidu et al., 2017). In addition to the change of the real dielectric constant according to the frequency, the change with contribution is also evident. An increase in the real part of dielectric constant was observed as the La^{3+} contribution increased. The value of the dielectric constant was about 2000 in the undoped sample, and it increased to more than an order and reached 54000 at x = 0.5 sample.

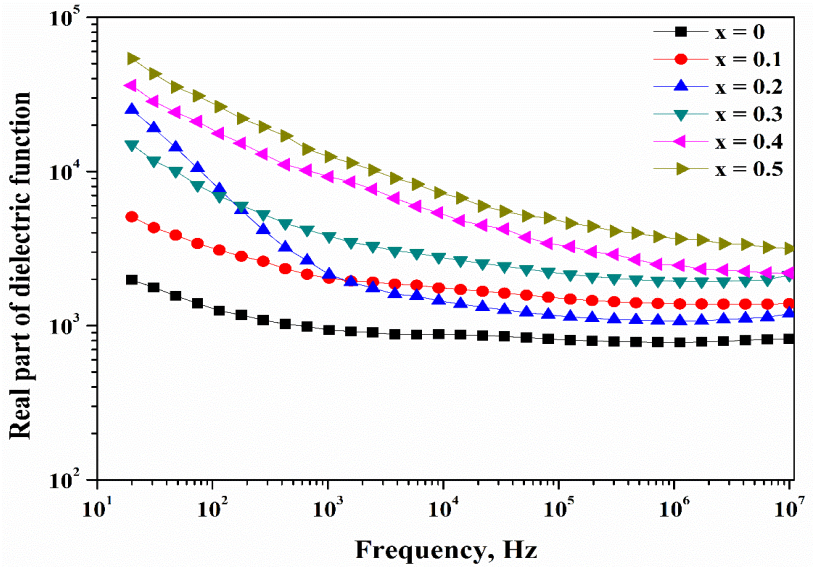

Figure.4. Variation of real part of dielectric function with frequency for all concentrations.

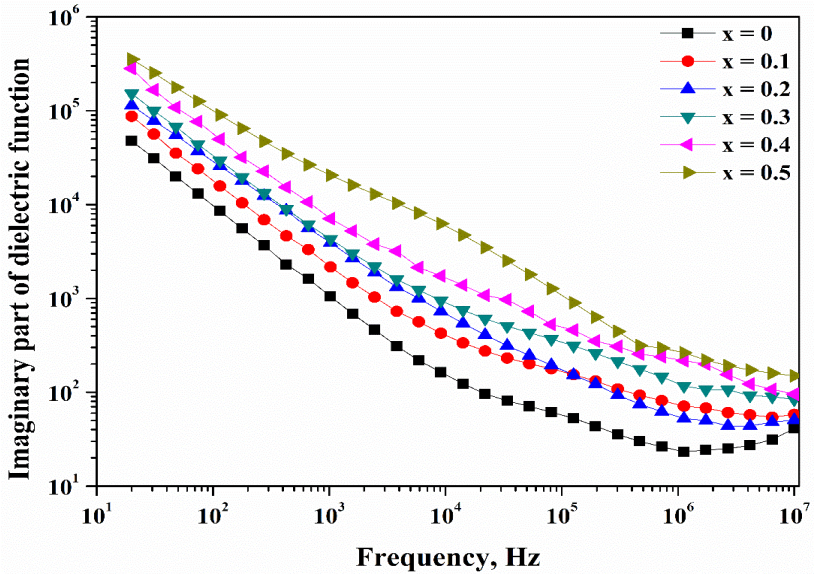

Figure.5. Frequency dependence of imaginary part of dielectric function for CoMgLa ferrites.

Imaginary part of dielectric constant, known as dielectric loss, consists of three parts, namely conduction losses, dipole losses and vibration losses (Jaidka et al., 2018; Polat et al., 2020). It is possible to explain the occurrence of dielectric loss in materials, the reduction of the charge storage capability by the independent movement of electric polarization with the changing electric field (Kuru et al., 2019). The Fig. 5 shows the change in the frequency of the dielectric loss. As with the dielectric constant, the dielectric loss decreased with increasing frequency in all samples. Because the grain boundaries are weak as conductors at low frequencies, more energy is needed for polarization. Thus, the energy loss is high. Furthermore, since the grains are better conductive, they require less energy for polarization at higher frequencies. This results in low dielectric loss. If these two different behaviors will be explained in another way: at low frequencies, the hopping mechanism of the charge carriers cannot be realized as it requires a lot of energy, while at high frequency region charge carriers need less energy to jump between the grains (Şaşmaz Kuru et al., 2018).

The loss tangent, $\tan\theta$, is obtained from the real ratio of the imaginary dielectric constant:

$$\tan\theta = \frac{\varepsilon''}{\varepsilon'} \quad (9)$$

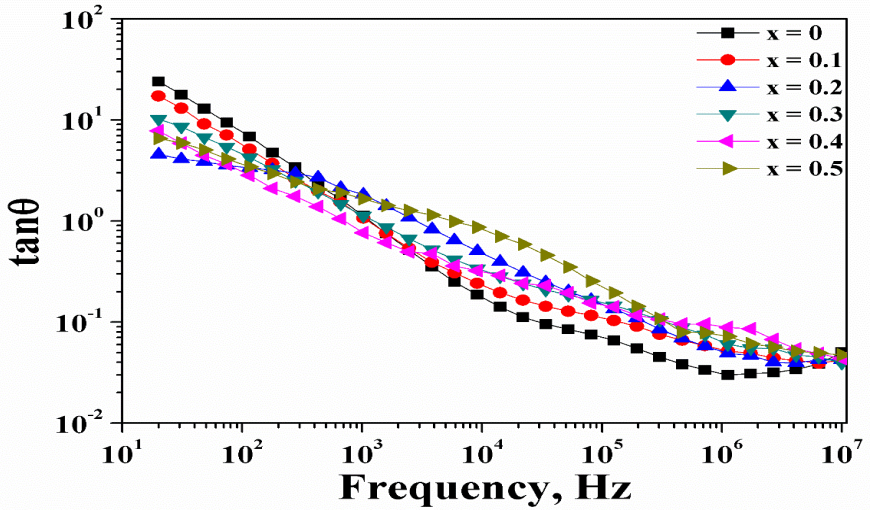

Figure.6. Frequency dependence of the tangent loss.

Fig. 6 shows the change of $\tan\theta$ with frequency. Generally, at almost all compositions, as the frequency increased, $\tan\theta$ decreased. This behavior is attributed to the relationship between the dielectric process and the conduction mechanism. The transmission mechanism is the electron jump between the cations. In ferrites, the distance between the A and B sites is too high, so there is little chance of hopping between the cations in these two sites. However, it is more likely to jump between neighboring B sites (Thomas et al., 2017). However, some x values have fluctuations rather than a linear decrease, and even peaks that can be called a relaxation peak. $\tan\theta$ has the highest value when the frequency of the hopping charge between the cations is equal to the applied frequency (Thomas et al., 2017). The change in $\tan\theta$ can be influenced by factors such as the composition of the material, preparation method and the amount of Fe^{2+} ions (Sharma et al., 2016). At high frequencies, the loss at all concentrations is almost same and the composition independent. This can be clarified by expanding the measuring range. Low losses at high frequencies indicate that these samples can be used in high frequency applications.

The impedance spectroscopy is an important method used to investigate the contribution of grain, grain boundary and material electrode interface to materials. The semicircle observed at low frequencies is formed by the contribution of grain boundaries, while the semicircle that occurs at high frequencies is formed by the contribution of grains. Fig. 7 shows the Nyquist plots of the samples. The fact that the center of the semicircle is below the real axis indicates that the relaxation process presence of non-Debye type but conforms to the Cole-Cole model. As seen clearly from the figure, all samples have a single semicircle. The appearance of a single semicircle leads to the conclusion that only grain boundaries are involved in the relaxation process (Mazen and Abu-El Saad, 2017). As a result of the semicircle obtained from the graph, the equivalent circuit of the samples can be easily modeled. Based on single half circles, it can be said that the equivalent circuit of the samples consists of capacitance and resistance connected in parallel to one another. The equivalent circuit is shown in Fig. 8. The relationship between the capacitance and resistance of grain boundaries is expressed by the following formula (Sekulić et al., 2016):

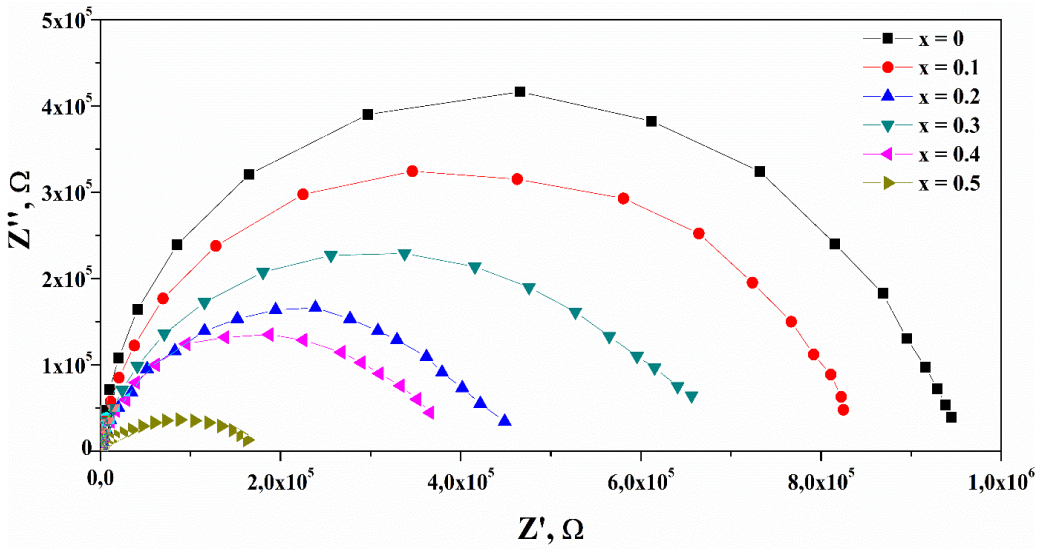

Figure.7. Cole–Cole plots of samples at room temperature.

$$C_{gb} = {}^{1}/_{R_{gb}\omega_{gb}} \quad (10)$$

where ω_{gb} is the frequency at the peaks of the semicircles for grain boundaries. Relaxation time can also be calculated by this equation,

$$\tau_{gb} = \frac{1}{\omega_{gb}} = C_{gb}R_{gb} \quad (11)$$

R_{gb} and C_{gb} values are given in Table 3 along with the relaxation times calculated according to Eq. 11.

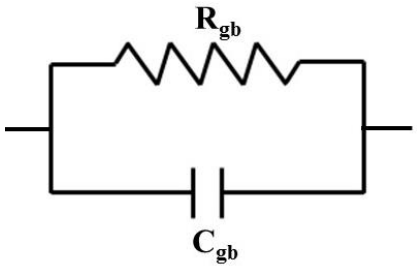

Fig. 8 The equivalent circuit of the relaxation process.

Table 3 Resistance, capacitance and relaxation times of grain boundaries.

x	R_{gb} × 10^5 (Ω)	C_{gb} × 10^{-10} (F)	τ_{gb} × 10^{-5} (s)
0	8.80	1.49	13.1
0.1	7.15	1.80	12.9
0.2	3.24	2.00	6.48
0.3	5.00	2.02	10.1
0.4	2.32	4.01	9.3
0.5	1.03	6.12	6.3

In addition to the dielectric constant and impedance, the electrical response of the materials can also be performed by electrical modulus analysis. This method offers an alternative approach based on polarization (Oumezzine et al., 2017). The frequency-dependent change of the real and imaginary parts of the modulus is a method used to examine the relaxation mechanism and compositional and structural dependence of the relaxation time of spinel ferrites (Kaiser, 2016; Yadav et al., 2017). The real (M') and imaginary (M'') parts of the complex electrical modulus are calculated by the following formulas:

$$M' = \omega C_0 Z'' \quad (12)$$

$$M'' = \omega C_0 Z' \quad (13)$$

$$C_0 = \frac{\varepsilon_0 A}{d} \quad (14)$$

where ω is angular frequency, C_0 is empty capacitance of the sample, Z' is real impedance and Z'' is imaginary impedance.

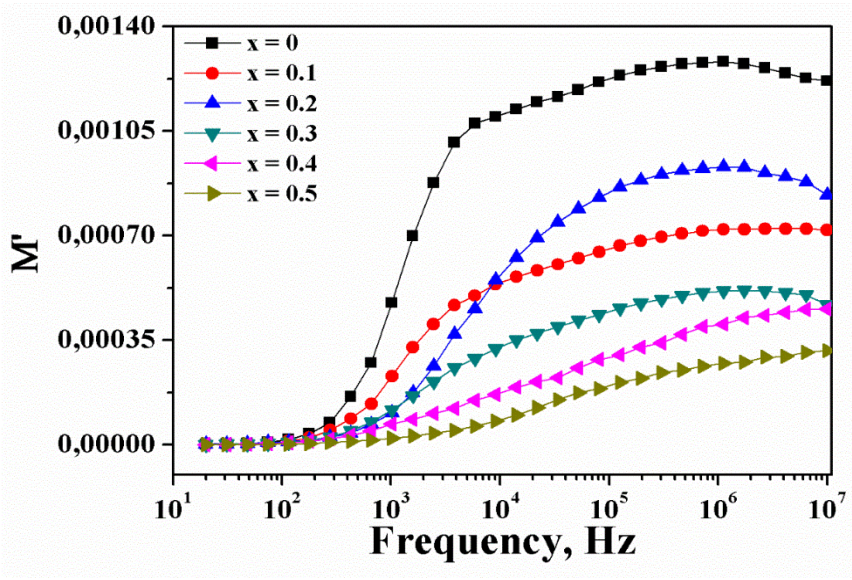

Figure.9. Frequency dependence of real modulus.

The frequency dependence of the real part of electrical modulus for all samples is shown in the Fig. 9. It was observed that M' was almost zero and frequency independent at low frequencies and increased with increasing frequency. At high frequencies, M' tends to reach a saturate maximum value caused by the relaxation process. This behavior is proof that the conduction process shows short-range mobility of charge carriers. Moreover, it indicates that there is no restoring force that provides the mobility of the charge carriers with the alternative electric field (Yadav et al., 2017). As x increased, the value of M' decreased and the shape of the curves became smoother. Also, the dispersion regions shifted to higher frequencies. However, as can be clearly seen from the figure, small M' values at low frequencies indicate the ease of polaron hopping (Kaiser, 2012). Performing modulus spectra analysis is advantageous in examining the differences between electrode polarization and grain boundary conduction process.

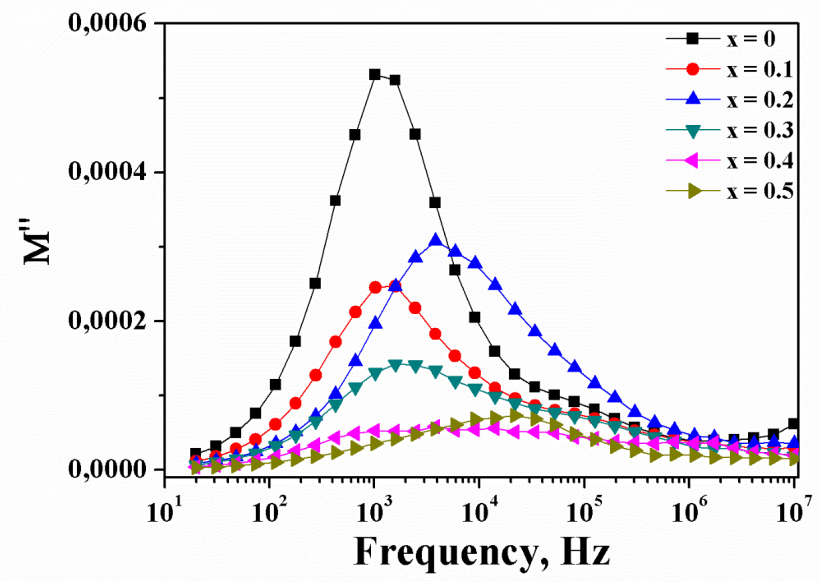

Figure.10. Imaginary modulus of the samples.

The imaginary part of the electrical modulus is characterized by a peak, and the peak position has shifted to high frequency regions with increasing x values shown in Fig. 10. This shift is attributed to the long-range mobility of the charge carriers (Kaiser, 2016). This shift indicates that the contribution of grain boundaries to resistance decreases with increasing La^{+3} ions concentration. It is also evident that the peak width gets wider with the increased x value. Asymmetric peak widths indicate the difference in relaxation times. The characteristic frequency of M'_{max} and M''_{max} are equal to the relaxation frequencies. This frequency (f_m) value is used to determine the relaxation times. The results obtained from the graph of the imaginary part of the modulus are compatible with the real part. While f<f_m charge carriers are mobile long distance, f>f_m they are mobile short distance. It is understood that the maximum frequency (characteristic frequency) f_m, indicates that the transition changes from long distance to short distance mobility (Kaiser, 2012).

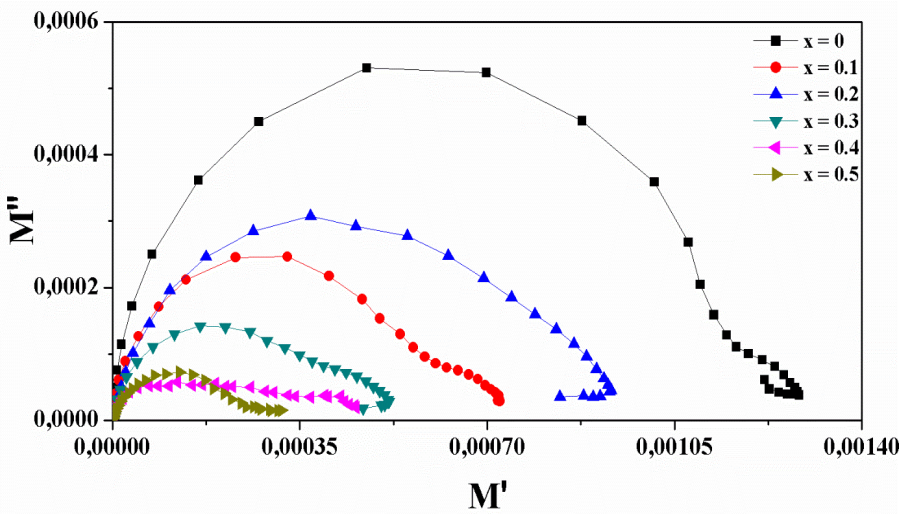

Figure.11. Cole-Cole diagrams of CoMgLa ferrites

While the imaginary impedance (Z'') determines the relaxation process of the materials with the greatest resistance, the imaginary modulus (M'') is related to the smallest capacitance. This indicates that the material is related to the most conductive parts. Therefore, the effect of grains on the relaxation process is more effective when it is performed by modulus examination instead of impedance

examination (Yadav et al., 2017). As seen from the Cole-Cole graph in Fig. 11 drawn by the modulus, the curves consist of one completed and one-half semicircles. The presence of half semicircle at high frequencies is evidence that the grains also contribute to the relaxation process in ferrite nanomaterials. This situation shows the contribution of both grains and grain boundaries to the relaxation process. The radius of the semicircle is related to the morphology and particle size of the samples (Yadav et al., 2017).

Such AC conductivity values are obtained by using the conductance data measured during the experiment and using the following formula:

$$\sigma_{AC} = \frac{Gd}{A} \quad (15)$$

where G is the electrical conductance, t is the thickness of the pellet, and A is the surface area of the pellet. In Fig. 12, it is obvious that the AC conductivity exhibits an almost independent behavior of the frequency at low frequencies and at low concentrations, while it is evident that it increases with increasing frequency and concentration. The frequency dependence of the AC conductivity can be explained by Koop's multi-layer theory, as in the dielectric mechanism (Gowreesan and Kumar, 2018). At low frequencies, the contribution of grain boundaries to conductivity is greater, while the grains contribution is higher at high frequency region. Therefore, the electron hopping between Fe^{+2} and Fe^{+3} ions at low frequencies is blocked and hence AC conductivity is almost constant. Therefore, conductivity for all samples has the lowest values at low frequencies. However, activation of the grains with increasing frequency facilitates the hopping of electrons. Thus, AC conductivity increases. It is called hopping-frequency where the conductivity starts to change from steady state to increasing state. This behavior of conductivity indicates that different types of hopping and charge carriers are involved in the transition process (Kaiser, 2012).

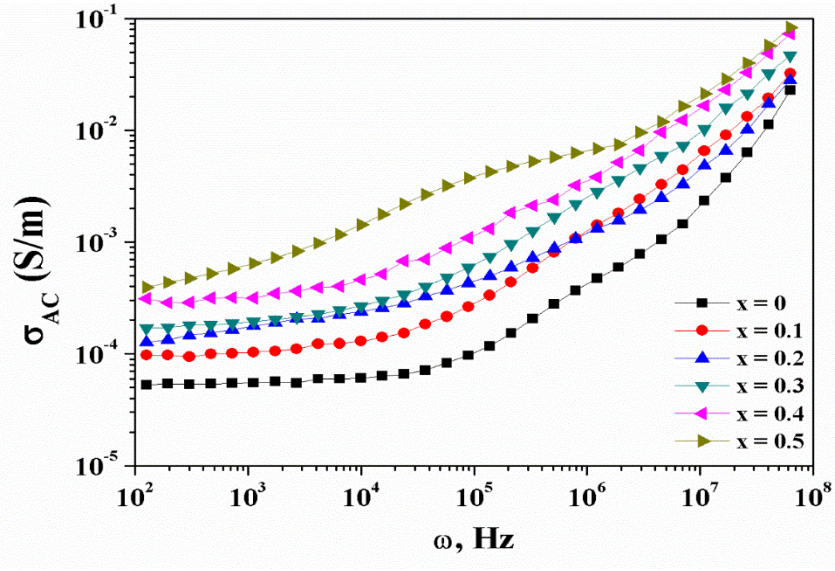

Figure.12. AC conductivity versus angular frequency

With increasing concentration of La^{3+}, the increase in conductivity is also observed. In addition to this, the conductivity values approached each other for all samples in the high frequency region. This situation can be interpreted as the localization of the electric charge (Kaiser, 2012). The ferrites are materials with low mobility and the increase in conductivity does not mean that the number of charge carriers increases. As the conductivity increases, only the mobility of the charge carriers increases (Oumezzine et al., 2017). The hopping length of the charge carriers is related to the energy required to

pass the barrier for jump from one cationic zone to another. The probability of electron hopping between the tetrahedral (A) sites and the octahedral (B) sites is lower than the probability of hopping between the two B zones. Because the electron needs more energy to jump from A-site to B-site. The hopping length for A-site and B-site can be calculated using the following formulas (Pervaiz and Gul, 2014):

$$L_A = a\frac{\sqrt{3}}{4} \quad (16)$$

$$L_B = a\frac{\sqrt{2}}{4} \quad (17)$$

where a is the lattice constant.

Table 4 The hopping lengths for A and B sites.

x	$\boldsymbol{a}$ (Å)	$\boldsymbol{L_A}$(Å)	$\boldsymbol{L_B}$(Å)
0.0	8.3556	3.618081	2.954151
0.1	8.3602	3.620073	2.955777
0.2	8.3648	3.622065	2.957403
0.3	8.3557	3.618124	2.954186
0.4	8.3693	3.624013	2.958994
0.5	8.3817	3.629383	2.963378

The calculated L_A and L_B values for all samples are listed in Table 4. As can be clearly seen from the table, L_A and L_B are increasing with increasing La^{3+} contribution. Increased lengths help us understand that more energy is needed for inter-site electron hopping. The graph of the hopping lengths versus the composition is shown in Fig. 13.

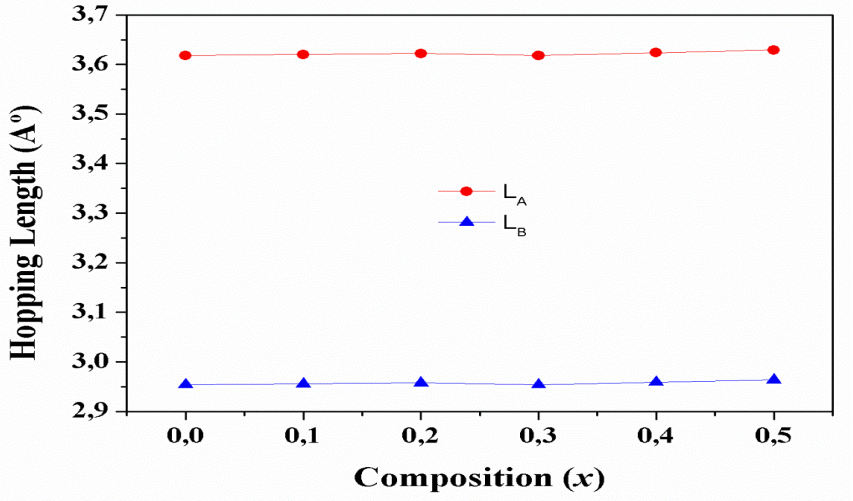

Figure.13. The composition dependency of hopping lengths for A and B sites.

CONCLUSION

X-ray powder diffraction patterns confirm the formation of cubic spinel phase with some $LaFeO_3$ impurities indicating successful synthesis of $Co_{0.5}Mg_{0.5}La_xFe_{2-x}O_4$ ($0.0 \leq x \leq 0.5$) by co-precipitation process. According to the results obtained from the XRD data, the crystal size ranged from 9.80 to 24.62 nm, while the lattice parameter increased from 8.3556 Å to 8.3817 Å with La^{3+} contribution. Based on

the SEM results, it was confirmed that the particles were generally nano-sized and EDX results show that the desired stoichiometry is obtained. Dielectric constant and dielectric loss decreased with increasing frequency with the range of 20 Hz to 10 MHz. This shows that the samples show normal dielectric behavior and are consistent with the Koops' phenomenological theory. As the frequency increases, the decrease in dielectric constant is quite low in the sample without additive, while the maximum amount of additive has highest decrease in the x = 0.5 sample. By analyzing the resistant parts of the samples with the impedance analysis, it was understood that the contribution to the relaxation process came from only the grain boundaries, while the capacitive parts of the samples were examined by the modulus analysis and the grains also played a role in the relaxation process. The semiconductor character of the CoMgLa ferrite materials is also confirmed by using Nyquist curves. These curves are an indication that the relaxation process is compatible with the Cole-Cole model. AC conductivity increased with increasing frequency and concentration.

REFERENCES

Ahmad I, Abbas T, Ziya AB, Abbas G, Maqsood A, 2014. Size dependent structural and magnetic properties of Al substituted Co–Mg ferrites synthesized by the sol–gel auto-combustion method. Materials Research Bulletin 52 11–14.

Ahmed MA, Ateia E, Salah LM, El-Gamal AA, 2005. Structural and electrical studies on La^{3+} substituted Ni–Zn ferrites. Materials Chemistry and Physics 92 (2–3) 310-321.

Ashtar M. Munir A, Anis-ur-Rehman M, Maqsood A, 2016. Effect of chromium substitution on the dielectric properties of mixed Ni-Zn ferrite prepared by WOWS sol–gel technique. Materials Research Bulletin 79 14–21.

Ciocarlan RG, Pui A, Gherca D, Virlan C, Dobromir M, Nica V, Craus ML, Gostin IN, Caltun O, Hempelman R, Cool P, 2016. Quaternary $M_{0.25}Cu_{0.25}Mg_{0.5}Fe_2O_4$ (M = Ni, Zn, Co, Mn) ferrite oxides: Synthesis, characterization and magnetic properties. Materials Research Bulletin 81 63–70.

Druc AC, Borhan AI, Diaconu A, Iordan AR, Nedelcu GG, Leontie L, Palamaru MN, 2014. How cobalt ions substitution changes the structure and dielectric properties of magnesium ferrite?. Ceramics International 40 13573–13578.

Gaba S, Kumar A, Rana PS, Arora M, 2018. Influence of La^{3+} ion doping on physical properties of magnesium nanoferrites for microwave absorption application. Journal of Magnetism and Magnetic Materials 460 69-77.

Gao J, Yan Z, Liu J, Zhang M, Guo M, 2015. Synthesis, structure and magnetic properties of Zn substituted Ni–Co–Mn–Mg ferrites. Materials Letters 141 122–124.

Ghodake UR, Chaudhari ND, Kambale RC, Patil JY, Suryavanshi SS, 2016. Effect of Mn^{2+} substitution on structural, magnetic, electric and dielectric properties of Mg–Zn ferrites. Journal of Magnetism and Magnetic Materials 407 60–68.

Ghodake UR, Kambale RC, Suryavanshi SS, 2017. Effect of Mn^{2+} substitution on structural, electrical transport and dielectric properties of Mg-Zn ferrites. Ceramics International 43 1129–1134.

Godlyn Abraham A, Manikandan A, Manikandan E, Vadivel S, Jaganathan SK, Baykal A, Sri Renganathan P, 2018. Enhanced magneto-optical and photo-catalytic properties of transition metal cobalt (Co^{2+} ions) doped spinel $MgFe_2O_4$ ferrite nanocomposites. Journal of Magnetism and Magnetic Materials 452 380–388.

Gowreesan S, Kumar AR, 2018. Synthesis, Structural, Dielectric and Magnetic properties of spinel structure of Ca^{2+} substitute in Cobalt Ferrites ($Co_{1-x}Ca_xFe_2O_4$). Chinese Journal of Physics 56 3 1262-1272.

Huang J, Su P, Wu W, Liu B, 2014. $Co_{0.5}Mn_{0.5}La_xFe_{2-x}O_4$ Magnetic Particles: Preparation and Kinetics Research of Thermal Transformation of the Precursor. Journal of Superconductivity and Novel Magnetism 27 (10) 2317–2326.

Ikram S, Imran Arshad M, Mahmood K, Ali A, Amin N, Ali N, 2018. Structural, magnetic and dielectric study of La^{3+} substituted $Cu_{0.8}Cd_{0.2}Fe_2O_4$ ferrite nanoparticles synthesized by the co-precipitation method. Journal of Alloys and Compounds 769 1019-1025.

Ishaque M, Khan MA, Ali I, Khan HM, Iqbal MA, Islam MU, Warsid MF, 2015. Investigations on structural, electrical and dielectric properties of yttrium substituted Mg-ferrites. Ceramics International 41 4028–4034.

Jadhav GL, More SD, Kale CM, Jadhav KM, 2018. Effect of Magnesium Substitution on the Structural, Morphological, Optical and Wettability properties of Cobalt Ferrite Thin Films. Physica B: Physics of Condensed Matter 555 61-68.

Jadoun P, Sharma J, Kumar S, Dolia SN, Bhatnagar D, Saxena VK, 2018. Structural and magnetic behavior of nanocrystalline Cr doped Co-Mg ferrite. Ceramics International 44 6747–6753.

Jaidka S, Khan S, Singh K, 2018. Na2O doped CeO2 and their structural, optical, conducting and dielectric properties. Physica B: Condensed Matter 550 189–198.

Kaiser M, 2012. Electrical conductivity and complex electric modulus of titanium doped nickel–zinc ferrites. Physica B 407 606–613.

Kaiser M, 2016. Magnetic and electric modulus properties of In substituted Mg–Mn–Cu ferrites. Materials Research Bulletin 73 452-458.

Kaur M, Jain P, Singh M, 2015. Studies on structural and magnetic properties of ternary cobalt magnesium zinc (CMZ) $Co_{0.6-x}Mg_xZn_{0.4}Fe_2O_4$ (x = 0.0, 0.2, 0.4, 0.6) ferrite nanoparticles. Materials Chemistry and Physics 162 332-339.

Köseoğlu Y, Oleiwi MIO, Yilgin R, Koçbay AN, 2012. Effect of chromium addition on the structural, morphological and magnetic properties of nano-crystalline cobalt ferrite system. Ceramics International 38 6671–6676.

Köseoğlu Y, Şentürk E, Eyüpoğlu V, Şaşmaz Kuru T, Hashim M, Meena SS, 2016. Structural, Conductivity, and Dielectric Properties of $Co_{0.5}Mg_{0.5}La_{0.1}Fe_{1.9}O_4$ Ferrite Nanoparticles. Journal of Superconductivity and Novel Magnetism, 29 2813-2819.

Kumar G, Sharma S, Kotnala RK, Shah J, Shirsath SE, Batoo KM, Singh M, 2013. Electric, dielectric and ac electrical conductivity study of nanocrystalline cobalt substituted Mg–Mn ferrites synthesized via solution combustion technique. Journal of Molecular Structure 1051 336–344.

Kuru M, Şaşmaz Kuru T, Bağcı S, 2019. The role of the calcium concentration effect on the structural and dielectric properties of mixed Ni–Zn ferrites. Journal of Materials Science: Materials in Electronics 30 (6) 5438-5453.

Li LZ, Zhong XX, Wang R, Tu XQ, 2017. Structural, magnetic and electrical properties of Zr-substitued NiZnCo ferrite nanopowders. Journal of Magnetism and Magnetic Materials 435 58–63.

Manikandan A, Durka M, Antony SA, 2015. Role of Mn^{2+} Doping on Structural, Morphological, and Opto-Magnetic Properties of Spinel $Mn_xCo_{1-x}Fe_2O_4$ (x = 0.0, 0.1, 0.2, 0.3, 0.4, and 0.5) Nanocatalysts. Journal of Superconductivity and Novel Magnetism, 28 2047–2058.

Mazen SA, Abu-ElsaadNI, 2017. Dielectric properties and impedance analysis of polycrystalline Li-Si ferrite prepared by high energy ball milling technique. Journal of Magnetism and Magnetic Materials 442 72–79.

Mund HS, Ahuja BL, 2017. Structural and magnetic properties of Mg doped cobalt ferrite nano particles prepared by sol-gel method. Materials Research Bulletin 85 228–233.

Naidu KCB, Kiran SR, Madhuri W, 2017. Investigations on transport, impedance and electromagnetic interference shielding properties of microwave processed NiMg ferrites. Materials Research Bulletin 89 125-138.

Oumezzine E, Hcini S, Rhouma FIH, Oumezzine M, 2017. Frequency and temperature dependence of conductance, impedance and electrical modulus studies of $Ni_{0.6}Cu_{0.4}Fe_2O_4$ spinel ferrite. Journal of Alloys and Compounds 726, 5 187-194.

Patil SB, Patil RP, Ghodake JS, Chougule BK, 2014. Temperature and frequency dependent dielectric properties of Ni–Mg–Zn–Co ferrites. Journal of Magnetism and Magnetic Materials 350 179–182.

Polat O, Coskun M, Coskun FM, Zlamal J, Durmus Z, Caglar M, Turut A, 2020. Influence of transition element Os substitution on the structural and electrical features of perovskite structure $LaCr_{1-x}Os_xO_3$. Materials Research Bulletin 124 110759.

Pawar RA, Patange SM, Tamboli QY, Ramanathan V, Shirsath SE, 2016. Spectroscopic, elastic and dielectric properties of Ho^{3+} substituted Co-Zn ferrites synthesized by sol-gel method. Ceramics International 42 16096–16102.

Pervaiz E, Gul IH, 2014. High frequency AC response, DC resistivity and magnetic studies of holmium substituted Ni-ferrite: A novel electromagnetic material. Journal of Magnetism and Magnetic Materials 349 27–34.

Rafiq MA, Khan MA, Asghar M, Ilyas SZ, Shakir I, Shahid M, Warsi MF, 2015. Influence of Co^{2+} on structural and electromagnetic properties of Mg–Zn nanocrystals synthesized via co-precipitation route. Ceramics International 41 10501–10505.

Ramarao K, Babu BR, Babu BK, Veeraiah V, Ramarao SD, Rajasekhar K, Rao AV, 2018. Composition dependence of structural, magnetic and electrical properties of Co substituted magnesium ferrite. Physica B: Physics of Condensed Matter 528 18–23.

Ramesh S, Dhanalakshmi B, Sekhar BC, Subba Rao PSV, Parvatheeswara Rao B, 2016. Effect of Mn/Co substitutions on the resistivity and dielectric properties of nickel–zinc ferrites. Ceramics International 42 9591–9598.

Rao P, Godbole R, Bhagwat S, 2016. Nanocrystalline Pd: $NiFe_2O_4$ thin films: A selective ethanol gas sensor. Journal of Magnetism and Magnetic Materials, 416 292-298.

Raut AV, Kurmude DV, Shengule DR, Jadhav KM, 2015. Effect of gamma irradiation on the structural and magnetic properties of Co–Zn spinel ferrite nanoparticles. Materials Research Bulletin 63123–128.

Ren X, Xu G, 2014. Electromagnetic and microwave absorbing properties of NiCoZn-ferrites doped with La^{3+}. Journal of Magnetism and Magnetic Materials 354 44–48.

Safi R, Ghasemi A, Shoja-Razavi R, 2016. Factors controlling magnetic properties of $CoFe_2O_4$ nanoparticles synthesized by chemical co-precipitation: Modeling and optimization using response surface methodology Ceramics International 42 15818–15825.

Sekulić DL, Lazarević ZZ, Jovalekić ČD, Milutinović AN, Romčević NZ, 2016. Impedance Spectroscopy of Nanocrystalline $MgFe_2O_4$ and $MnFe_2O_4$ Ferrite Ceramics: Effect of Grain Boundaries on the Electrical Properties. Science of Sintering, 48 17-28.

Sharma J, Sharma N, Parashar J, Saxena VK, Bhatnagar D, Sharma KB, 2015. Dielectric properties of nanocrystalline Co-Mg ferrites. Journal of Alloys and Compounds 649 362-367.

Sharma R, Thakur P, Kumar M, Thakur N, Negi NS, Sharma P, Sharma V, 2016. Improvement in magnetic behaviour of cobalt doped magnesium zinc nano-ferrites via co-precipitation route. Journal of Alloys and Compounds 684 569-581.

Shinde TJ, Gadkari AB, Vasambekar PN, 2010. Effect of Nd^{3+} substitution on structural and electrical properties of nanocrystalline zinc ferrite. Journal of Magnetism and Magnetic Materials 322 2777–2781.

Sun L, Zhang R, Ni Q, Cao E, Hao W, Zhang Y, Ju L, 2018. Magnetic and dielectric properties of $Mg_xCo_{1-x}Fe_2O_4$ ferrites prepared by the sol-gel method. Physica B: Condensed Matter 545 4–11.

Sundararajan M, Kennedy LJ, Nithya P, Vijaya JJ, Bououdina M, 2017. Visible light driven photocatalytic degradation of rhodamine B using Mg doped cobalt ferrite spinel nanoparticles synthesized by microwave combustion method. Journal of Physics and Chemistry of Solids 108 61–75.

Sutka A, Gross KA, 2016. Spinel ferrite oxide semiconductor gas sensors. Sensors and Actuators B 222 95–105.

Şaşmaz Kuru T, Şentürk E, 2016. Humidity sensing properties of ferrite based Al-Cd nanoparticles as a fast response sensor device. Sensors and Actuators A 249 62–67.

Şaşmaz Kuru T, Şentürk E, Eyüpoğlu V, 2017. Overlapping Large Polaron Conductivity Mechanism and Dielectric Properties of $Al_{0.2}Cd_{0.8}Fe_2O_4$ Ferrite Nanocomposite, Journal of Superconductivity and Novel Magnetism 30, 647-655.

Şaşmaz Kuru T, Kuru M, Bağcı S, 2018. Dielectric, humidity behavior and conductivity mechanism of $Mn_{0.2}Ni_{0.3}Zn_{0.5}Fe_2O_4$ ferrite prepared by co-precipitation method. Journal of Materials Science: Materials in Electronics 29 17160-17169.

Thomas N, Jithin PV, Sudheesh VD, Sebastian V, 2017. Magnetic and dielectric properties of magnesium substituted cobalt ferrite samples synthesized via one step calcination free solution combustion method. Ceramics International 43 7305–7310.

Vasoya NH, Jha PK, Saija KG, Dolia SN, Zankat KB, Modi KB, 2016. Electric Modulus, Scaling and Modeling of Dielectric Properties for Mn^{2+}-Si^{4+} Co-substituted Mn-Zn Ferrites. Journal of Electronic Materials, 45(2) 917-927.

Wu X, Wu W, Qin L, Wang K, Ou S, Zhou K, Fan Y, 2015. Structure and magnetic properties evolution of nickel-zinc ferrite with lanthanum substitution. Journal of Magnetism and Magnetic Materials 379 232–238.

Yadav RS, Kuřitka I, Vilcakova J, Urbánek P, Machovsky M, Masař M, Holek M, 2017. Structural, magnetic, optical, dielectric, electrical and modulus spectroscopic characteristics of $ZnFe_2O_4$ spinel ferrite nanoparticles synthesized via honey-mediated sol-gel combustion method. Journal of Physics and Chemistry of Solids 110 87–99.

Yadav RS, Kuřitka I, Vilcakova J, Havlica J, Masilko J, Kalina L, Tkacz J, Enev V, Hajdúchová M, 2017. Structural, magnetic, dielectric, and electrical properties of $NiFe_2O_4$ spinel ferrite nanoparticles prepared by honey-mediated sol-gel combustion. Journal of Physics and Chemistry of Solids 107 150-161.

Yang Y, Li M, Ren Y, Li Y, Xia C, 2018. Magnesium oxide as synergistic catalyst for oxygen reduction reaction on strontium doped lanthanum cobalt ferrite. International Journal of Hydrogen Energy 43 (7) 3797-3802.